Laser Terahertz Emission Near-field Microscopy

Amy L. Butcher
advised by
Prof. Daniel Mittleman

A thesis completed in partial fulfillment
of the requirements for the degree of
Bachelor of Science
in
Engineering Physics
Brown University

May 4, 2017

Abstract

Laser terahertz emission microscopy (LTEM) maps the generation of terahertz radiation by ultrafast photo-excitation of charge carriers. Capable of visualizing factors affecting THz emission such as supercurrent distributions, ferroelectric domains, and local electric fields, this technique has recently been used to nondestructively detect faults in integrated circuits. Conventional LTEM is diffraction-limited and thus unable to resolve nanoscale structures which determine the macroscopic behavior of many materials and which comprise modern electronics. To increase the resolution of terahertz emission microscopy, we developed a scattering near-field microscope which employs a metal tip to probe THz emission from nanoscale sample regions.

This thesis presents the current status of the instrument, investigates the differences between conventional and near-field LTEM, and explores THz emission differences between various doped semiconductor materials. I find that, unlike previous studies using scattering near-field techniques for THz spectroscopy, the near-field probe in this case does not limit detected THz bandwidth. The nonlinear nature of LTEM complicates common definitions of resolution and contrast, yet this system exhibits resolution comparable to AFM topography (10-20nm). Near-field LTEM opens the door to diffraction unlimited investigations of THz emission and we anticipate future studies of individual nanodevice characteristics using this technique.

Contents

1 Nano-optical microscopy

Of all the scientific tools at our disposal, light may be the most familiar. We are accustomed to interpreting light-based phenomena, at least on the macroscale, because we rely heavily on our sense of sight to investigate our surroundings. This fundamental intuition already makes optical microscopy an attractive scientific technique. More important from a physicist's point of view is that the broad energy range of light corresponds to electronic, spin, and lattice excitations in materials. This compatibility means that light-matter interactions can reveal a material's properties while also providing a means to manipulate its quantum states. The spectroscopic capabilities of optical microscopy abound, with lasers and nonlinear frequency generation– and the more recent development of high power terahertz sources– providing an enormous range of energies for experimental use. That said, the magnification capability of conventional optical microscopy is necessarily limited because light is wave-like. Light in the visible spectrum, for example, can resolve structures only down to a few hundred nanometers in size. Since the macroscopic properties of functional materials are determined by structures and dynamics which occur below this scale, it remains important to transcend this limitation, a goal that is more relevant than ever given contemporary interest in nanotechnology.

In this section I discuss the resolution limit of conventional microscopic imaging and then introduce near-field optics as a solution to this problem. Special attention is given to tip-enhanced imaging and relevant experimental considerations.

1.1 The Diffraction Limit

The need for near-field microscopy falls naturally out of a discussion of the resolution limit for conventional (also called far-field) microscopy. Spatial resolution measures the minimum separation at which two point sources can be distinguished. A point source of light in the plane $z = 0$ is characterized by a two-dimensional delta function in x and y, which constitutes an infinite spectrum of spatial frequencies k_x and k_y. This reciprocal relationship is given by $\Delta k \Delta r = 1$, where Δk represents a bandwidth of spatial frequencies and Δr represents position uncertainty. If all of these frequencies propagated equivalently in z, then the image of a point source would still be an exact point in any other z-plane. However, as light propagates in free space, the magnitude of its wavevector must satisfy $k_x^2 + k_y^2 + k_z^2 = |\mathbf{k}|^2 =$

$(w/c)^2$. This equation encapsulates the wave nature of light, and it is the relationship from which the diffraction limit is derived. Spatial frequencies for which $k_x^2 + k_y^2 = k_\parallel^2 > |\mathbf{k}|^2$ correspond to imaginary values of k_z. Since an imaginary k_z corresponds to exponential decay rather than an oscillating, propagating field, the electric fields associated with high k_x and k_y values decay in the z direction. Propagation essentially acts as a low pass filter on spatial frequency. With a reduced bandwidth of spatial frequencies, a point source appears to have finite size when viewed in a plane $z = z_0 > 0$. Its image blurs. As two blurry-looking point sources are brought near one another, they eventually become unresolvable.

If the light is further spatially filtered by a collection apparatus like an aperture or lens, the resolution limit is further tightened based on the efficiency (or numerical aperture, NA) of the collection optic. Given this practical consideration, the foregoing discussion of point sources, and the relationship $k = 2\pi/\lambda$ between spatial frequency and wavelength, the diffraction limit can be expressed as:

$$\Delta r_{min} = \frac{\lambda}{2\pi NA} \tag{1}$$

where Δr_{min} represents the minimum resolvable separation of two point sources in a plane. NA values are usually less than 1.0 and do not exceed 1.4 in practice.

The conclusion we must draw is that spatial resolution is limited to a few hundred nanometers for visible light. Terahertz microscopy is especially impaired since the relevant wavelength range is a thousand times larger than visible light, and resolution is therefore restricted to hundreds of microns. Techniques to overcome this limitation are the domain of near-field optics.

1.2 Near-field Optics

The ambition of near-field optics is to retain information that is typically lost with the decay of high spatial frequencies. "Near-field" refers to the region in which evanescent waves are significant, typically a layer tens of nanometers from illuminated sample surfaces. In order to access information stored in the near-field, a probe is brought into the region, which functions to confine radiation in a small area over the sample surface and to interact with near-field optical components from the sample. This probe-sample interaction encodes near-field information into radiation which either scatters off or is transmitted through the probe. Thus, near-field information is transferred to the far field, where it may be detected. By

scanning the probe over the sample surface, an image may be formed with contrast given by differences in near-field signal due to surface features. Resolution is generally limited by the size and properties of the probe object rather than the wavelength of light being used, which bypasses the diffraction limit.

Ultrahigh resolution comes at a cost, as the probing object and sample must be coupled, unlike in conventional microscopy. Any analysis of the sample's optical properties must consider the probe-sample interaction. Also important to consider is the necessary trade-off between light confinement and overall signal levels. Since the sample region being probed is very small and near-field optical components represent only a portion of the total electric field at the probe, near-field signal must be carefully discriminated from background and noise. Additionally, because the probe object cannot, in general, enter the bulk of the sample, near-field microscopy is confined to surface studies.

Even with these complications, near-field microscopy is an enormously powerful experimental technique. Just as the first telescopes created a new paradigm for astrophysical research in the seventeenth century, the development of nano-optics has opened fresh avenues of inquiry for scientists working on the meso- and nanoscale today. Recent examples include visualizing surface plasmons in low dimensional electronic materials, characterizing phase separation in transition metal oxides [2], and infrared imaging of molecular structures in soft materials [4].

Although the first proposal of diffraction unlimited microscopy dates back to the 1920s, the technique did not become experimentally feasible until the mid-1980s [2]. Three key technological developments made near-field microscopy possible. First, the development of high power lasers provided the intense illumination necessary to achieve measurable near-field signals. Second, piezoelectric scanner-positioners granted sub-nanometer spatial control. This precision led to the development of scanning tunnelling and atomic force microscopy, which served as a platform for near-field experiments. Third, advances in microfabrication made it possible to create various sub-wavelength sized near-field probes.

The first realization of near-field optical microscopy used a metal-coated quartz crystal with a 30nm apex as an aperture probe [3]. This 1984 experiment yielded an unprecedented 25nm spatial resolution with 488nm wavelength light. Later, aperture probes were created by coating tapered optical fiber tips with metal, which provided an easy way to excite underlying samples. The spectral range of this technique is limited, however, since optical fibers

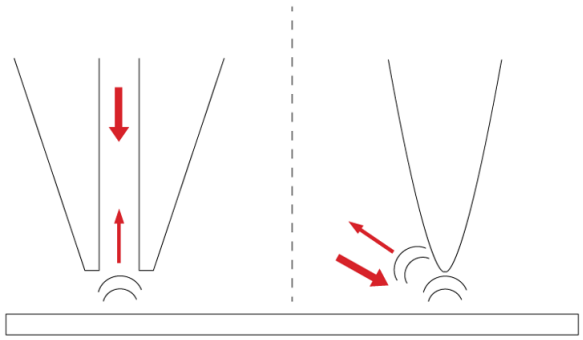

Figure 1: Aperture based microscopy (left) uses an optical fiber to both direct incident radiation and collect near-field signal, while s-SNOM (right) mediates the near-field interaction through scattering of incident radiation at a tip apex.

generally allow visible and infrared frequencies only. Moreover, the resolution achievable with an aperture probe is limited because the diameter of an aperture cannot be less than two times the skin depth of its metal coating. Apertures therefore cannot be smaller than a few tens of nanometers, since skin depths are typically 6-10nm [1]. Additionally, only a small amount of light may be transmitted through a nano-aperture, which diminishes maximal signal levels. In response to these issues, scattering based near-field microscopy was developed during the 1990s.

1.3 Scattering Scanning Near-field Optical Microscopy (s-SNOM)

In s-SNOM, incident radiation is confined and enhanced over a nanoscale region of a sample surface by a metal tip. Field enhancement is due to a combination of the plasmonic response in the metal tip and field line crowding (the "lightning rod effect") at its sharp apex [1]. Figure 2 includes a depiction of this field enhancement. The near-field contrast mechanism in s-SNOM is due to dipole coupling between tip and sample, which is sensitive to the dielectric function of the sample. Modelling the tip apex as a polarizable sphere reveals that tip radius is the primary factor which determines spatial resolution. With today's fabrication technology producing tips with radii as small as 10nm, s-SNOM resolution exceeds that of aperture-based microscopy [2].

Scanning control during s-SNOM experiments is provided by an atomic force microscope. Commercial AFM tips (pictured in Figure 2) make excellent near-field probes and a variety

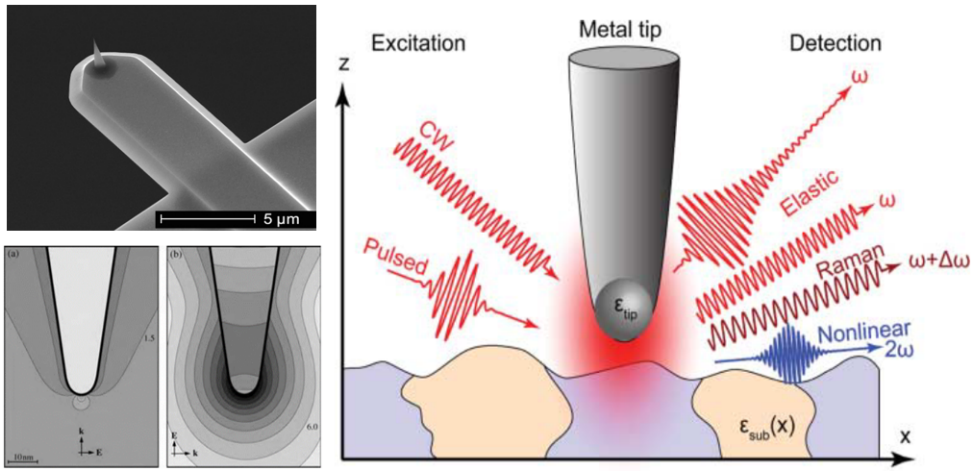

Figure 2: Top left: SEM image of commercial AFM tip (from NanoAndMore USA) on flexible cantilever. Bottom left: Field enhancement at a metal tip apex for horizontally (left) vertically (right) polarized light. Lines depict factors of two in electric field amplitude [1]. Right: An enormous range of spectroscopic s-SNOM studies are possible, with contrast arising from tip-sample dipole interactions [2].

are available, with different plasmonic resonances depending on tip length. The AFM is typically used in tapping mode, where the tip is oscillated by driving the AFM cantilever near its resonance frequency. As a result, the tip oscillates vertically with an amplitude of tens of nanometers near the sample surface. One benefit of using tapping mode is that the tip is in surface contact for less time, reducing tip deterioration which decreases resolution. Crucially, tip oscillation also provides a way to discriminate near-field signal from background. Because evanescent waves decay nonlinearly, they contribute to signals at higher harmonics of the tapping frequency, where background contributions are generally not present. By using lock-in amplification at these higher frequencies, a signal exponentially decaying near-field signal may be isolated.

Tip-enhanced microscopy is compatible with virtually any wavelength and spectroscopic technique. As a result, s-SNOM has found an enormous range of applications that include both linear and nonlinear, pulsed and continuous wave, and Raman and elastic spectroscopy. This compatibility is also the reason why s-SNOM is a good candidate for THz microscopy.

2 The Terahertz Regime

With frequencies lying between electronic and optical regimes, terahertz radiation is the intermediary between the microwave and infrared portions of the electromagnetic spectrum. Long referred to as the "terahertz gap" because of the lack of sources and detectors operating in this range, it is only in the last few decades that THz frequencies have become accessible to researchers. Notably, the development of ultrafast lasers during the 1980s revealed that a variety of systems are capable of generating terahertz radiation following femtosecond optical excitation, including photoconductive antennas on semiconductor surfaces. Today the THz regime can be roughly defined as the range from 0.1-10 THz, and there is an increasing range of techniques for its generation and detection [5], [6], [7].

Unique aspects of THz include the transparency of most insulators and the strong vibrational absorption of water molecules at these frequencies [7]. This range corresponds to energies on the scale of roughly 0.4 - 40 meV and can excite bound charges, charge plasmas, molecular dipoles, and phonons in crystalline solids while being low enough in energy to remain non-ionizing and hence non-destructive [10]. This feature has led many to seek applications in non-invasive imaging and quality inspection. Meanwhile, the potential for fast transmission of large quantities of data is driving the exciting field of THz communication. Although it is beyond the scope of this thesis to provide a comprehensive review of THz science and technology, discussions of communication [9], spectroscopy [8], and imaging [11] applications for THz can be found elsewhere [12].

For the purposes of this work, THz radiation is a valuable tool that provides insight into charge carrier dynamics in solid materials. In the following section I introduce the most widespread technique in THz optoelectronics: time domain spectroscopy. I then discuss mechanisms that produce terahertz radiation at semiconductor surfaces and present laser terahertz emission microscopy, an imaging technique that maps THz pulse generation.

2.1 THz Time Domain Spectroscopy (TDS)

Terahertz time domain spectroscopy (THz-TDS) relies on the generation and detection of single-cycle pulses on picosecond timescales. A typical setup begins with a femtosecond optical laser, which produces pulses at a repetition rate of ≈100MHz. This train of optical pulses is split by a beam splitter, one half proceeding to generate THz pulses and the other

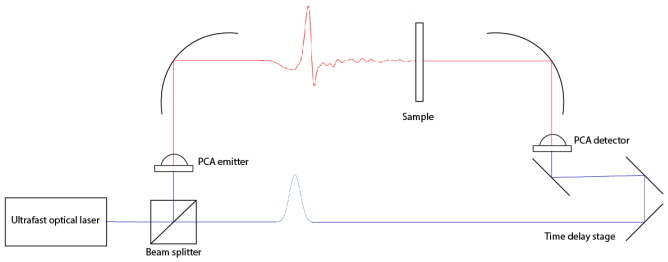

Figure 3: Schematic of a THz time domain spectroscopy system using gated photoconductive antennas for emission and detection.

half used to gate a detector. Between emitter and detector, a sample interacts with the THz pulses, changing their frequency-dependent amplitude and phase based on energy transitions in the material. Since the detector is sensitive to THz fields for a very short time (less than a picosecond) after it is gated by an optical pulse, there is a fleeting window in which the received THz electric field is measured. Assuming all generated THz pulses are identical, we can measure the pulse at various delays relative to its arrival at the detector to map its entire cycle. This time-domain approach essentially averages the shape of many THz pulses after they interact with a sample to yield spectroscopic information [11].

Emitters used in TDS experiments must be stable, the optical pulses used to gate detectors must be synchronized with the THz field, and detectors must be sensitive to the THz field for less than one picosecond at a time. With these constraints, photoconductive antennas (PCAs) have become the dominant method for emission and detection in TDS setups. PCAs use a metal antenna to maximize the generation of THz by optical pulses at semiconductor surfaces (described in the next section). Biased with a large electric field, this antenna enhances the current which is responsible for THz generation and couples emitted pulses into free space. At the detecting end, the THz electric field induces current in a gated PCA during a brief time window. PCAs sample the electric field directly, so the full oscillation of the pulse (both positive and negative fields) is resolved [10]. This full pulse detection is a departure from typical optical detection schemes, which measure intensity rather than electric field.

Since its development in the early 1990s, THz-TDS has been used to probe a considerable range of physical, chemical, and biological systems. Examples include the detection of illicit drugs and explosives concealed by insulators, investigations of transport properties in

semiconductors, and determination of water content in biological samples. For a review of some of these applications, see [10], [12].

In the case of semiconductor materials, TDS is a valuable tool for determining optical properties of samples in the THz range, from which electrical properties may be extracted. By comparing a reference pulse to one transmitted through a sample, the following transfer function can be found:

$$\frac{E_{samp}(\omega)}{E_{ref}(\omega)} = t(\omega)e^{i\phi(\omega)} \tag{2}$$

where $t(\omega)$ and $\phi(\omega)$, the transmittance and phase, are both frequency dependent. These quantities are related through Fresnel coefficients to a sample's complex index of refraction:

$$n(\omega) = 1 + \frac{\phi(\omega)c}{\omega d} \tag{3}$$

$$\alpha(\omega) = -\frac{2}{d}\ln\left(\frac{(n+1)^2}{4n}T(\omega)\right) \tag{4}$$

where $\tilde{n}(\omega) = n(\omega) + i\alpha(\omega)c/2\omega$ and d represents sample thickness [10]. Care must be taken when unwrapping the frequency dependent phase to calculate these values. A description of this unwrapping procedure can be found here [14]. Transmission mode measurements are also quite sensitive to the sample thickness, and are difficult to carry out if a sample is optically thick in the THz spectral range. For example, transmittance through heavily doped semiconductors is very low in this regime due to absorption by free carriers [13], [15].

Reflection mode TDS is a good alternative when transmitted power is too low for analysis using the equations above. In reflection based experiments, a highly reflective surface provides the reference signal, which is then replaced by a sample. Measurements in this case are very sensitive to sample placement, which ought to be at precisely the same position and angle as the reference surface. The optical constants are then given by:

$$n(\omega) = \frac{1-|r|^2}{1+|r|^2-2|r|\cos\phi(\omega)} \tag{5}$$

$$\alpha(\omega) = \frac{2\omega}{c}\frac{2|r|\sin\phi(\omega)}{1+|r|^2-2|r|\cos\phi(\omega)} \tag{6}$$

with r representing the Fresnel reflection coefficient at the sample surface, which depends on incident angle and polarization. For incident radiation polarized parallel to the plane of incidence,

$$r = \frac{\tan(\theta_i - \theta_t)}{\tan(\theta_i + \theta_t)} \tag{7}$$

where θ_i represents incident angle and θ_t represents the angle formed by the transmitted ray through the sample, which is in turn dependent on index of refraction.

Once the complex index of refraction has been calculated, the conductivity of a semiconductor sample can be found using the Drude model. Several studies have shown the accuracy of this model in the THz regime for semiconductors [15] [13]. The following equation connects optical and electronic properties:

$$\tilde{n}(\omega)^2 = \tilde{\epsilon} = \epsilon + \frac{4\pi i \sigma(\omega)}{\omega} \tag{8}$$

where ϵ represents the dielectric constant of the undoped semiconductor material, and σ represents the DC conductivity due to free carriers. With this relationship, TDS is an effective means to characterize the optoelectronic response of semiconductor samples in the THz regime.

2.2 THz Emission at Semiconductor Surfaces

Returning to the topic of THz pulse generation, two principle mechanisms exist for the generation of terahertz radiation from semiconductor surfaces: nonlinear optical rectification and surge current excitation. Here I focus on the latter, as it is the process responsible for THz generation in this work. A thorough review of both of these processes as well as plasmonic and phononic considerations is found in the chapter by Gu and Tani in [7].

In the case of terahertz generation due to surge current, the mechanism is as follows. An incident optical pulse (of central wavelength typically 800nm with a pulse duration less than 100fs) excites electrons into the conduction band of a semiconductor. After excitation, electrons and holes accelerate in opposite directions under the influence of an electric field and thus produce a time varying drift current. The electric field may be supplied by a surface depletion field or an external bias (as in photoconductive antennas, discussed in the previous section). Alternatively, diffusion current may be created after photoexcitation due to the difference in electron and hole mobilities, which is referred to as the photo-Dember effect. In actuality, both of these effects may be present to varying degrees based on the band structure and doping parameters of an individual sample. The amplitude of emitted

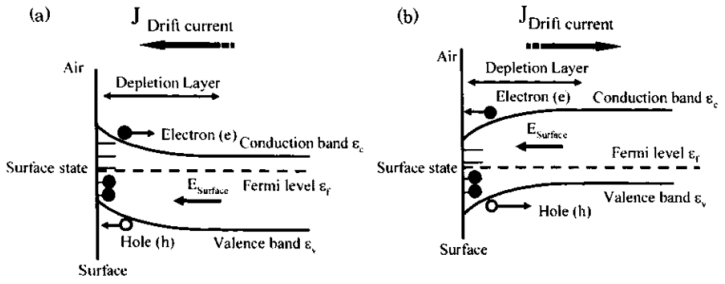

Figure 4: Illustration of photoexcited drift current that generates THz radiation in (a) n-type and (b) p-type semiconductors, from [7].

THz radiation in either case is proportional to the time derivative of the surge current:

$$E_{THz} \propto \frac{\partial J}{\partial t} \tag{9}$$

Creation of drift current due to surface depletion layers in n-type and p-type semiconductors is shown in Figure 4. A depletion layer forms at the surface of wide bandgap semiconductors because their surface state energies fall within the bandgap, leading to "Fermi level pinning" [7]. Essentially, electronic bands bend up at the surface in n-type semiconductors and down for p-type. The polarity of THz pulses emitted due to drift currents therefore depends on whether the semiconductor is n-type or p-type, as the direction of band bending determines the direction in which charges accelerate.

Conversely, when diffusion current is the principal generator of THz radiation, the polarity of the waveform is the same regardless of whether holes or electrons are majority carriers. This feature is due to the fact that the mobility of electrons is generally greater than the mobility of holes, as depicted in Figure 5. Since the density of photocreated electrons and holes is largest at the semiconductor-air interface, excited charge carriers diffuse away from the surface in all cases.

Previous work has investigated the factors which influence THz emission from InAs, InSb, and GaAs and the primary mechanisms responsible in each material [16], [17], [18]. Emission from InAs is strongly influenced by doping concentration because of screening effects [16]. InAs wafers with lower doping concentrations and lower majority carrier mobilities (i.e. p-type wafers) yield higher power THz radiation because of reduced screening

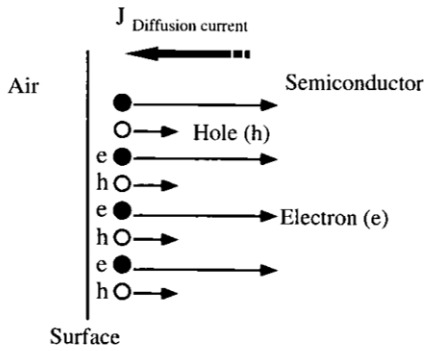

Figure 5: Illustration of the photo-Dember effect, in which diffusion current is created due to electron mobility exceeding that of holes [7].

by mobile carriers. InSb meanwhile provides a much lower emission efficiency than InAs, according to [17], which may be related to its larger electron mobility. Both InAs and InSb are narrow bandgap materials (0.34eV and 0.17eV, respectively), and are therefore both primarily dominated by the photo-Dember effect. In GaAs, a wide bandgap (1.43eV) material, this effect is negligible at room temperature. Emission is instead due to the influence of a surface depletion field, though the relative strength of the two emission mechanisms depends on carrier temperature [18].

Silicon, the most pervasive material in modern electronics, does not generate significant THz radiation for several reasons. Firstly, Si has an indirect bandgap, unlike the materials previously discussed. This feature means that fewer electrons are photoexcited by incident optical pulses. Si also does not exhibit band bending at its surface in air, which means there is no depletion layer to provide a built-in electric field for carrier acceleration. Finally, the mobility difference of holes and electrons in Si is orders of magnitude smaller than that in InAs, which means the photo-Dember effect is not significant in this material. That said, external fields are still capable of accelerating charges in Si, so THz emission can still be achieved with applied voltage.

2.3 Laser THz Emission Microscopy (LTEM)

Unlike THz-TDS, which maps a spectroscopic response to incident radiation, LTEM maps a sample's ability to generate THz. In addition to semiconductors, a variety of other electronic

materials emit THz radiation due to the acceleration of photo-excited charge carriers. Any sample capable of ultrafast current modulation may create THz waves by Equation 8. LTEM exploits this property to map supercurrent distributions, ferroelectric domains, and other local electric fields, all of which influence characteristics of THz pulse emission [19].

In a basic LTEM system, optical pulses are focused directly onto a sample which is mounted on a scanning stage. Emitted THz pulses may be detected on the opposite sample surface (transmission mode) or on the same side (reflection mode), while a time delay stage allows the entire pulse to be mapped, as in THz-TDS. The sample is raster scanned, with THz pulse detection occurring at each position on its surface. Taking the amplitude of this detected pulse as a contrast mechanism, an image is formed with each pixel representing one detected pulse. Spatial resolution is determined by the optical laser spot size, as this quantity determines the sample volume that is probed. Notably, this diffraction-limited resolution is considerably better than what is achievable with a THz spot because of the shorter optical wavelength (recall Equation 1).

Due to the sensitivity of LTEM to local electric fields, this technique has recently attracted attention as a means to diagnose faults in integrated circuits during operation. Various metal-semiconductor interfaces in these devices create band-bending which is mapped by LTEM, allowing circuit features to be imaged. By imaging circuits before and after they are intentionally damaged, researchers have shown that the polarity and amplitude of THz emission can be used as a tool to detect and diagnose faults [20]. Unlike other diagnostic tools that are commonly used for this purpose, LTEM is both non-contact and non-destructive to the underlying device.

Basic LTEM systems, being limited by diffraction, cannot resolve nanoscale structures which are ubiquitous in contemporary electronics. Improvements in spatial resolution would make LTEM a more valuable tool, one capable of visualizing the dynamic photo-response of semiconductor nanostructures. In order to achieve this ultrahigh resolution, we turn to near-field optics.

3 Terahertz Near-field Review

Terahertz science and near-field optics have developed alongside one another for the past thirty years. 1984 saw the first experimental realization of near-field microscopy as well as

the invention of the first photoconductive switches that enabled compact THz generation and detection [2], [7]. Today, integration of THz and near-field techniques is especially in demand due to technology's trend toward the nanoscale. Here I briefly review previous experiments that combined these fields, including spectroscopic (TDS) as well as LTEM-based work.

The first experimental realization of near-field imaging in the THz regime came in 1998 and used a tapered metal aperture in contact with a sample to reduce the THz illumination spot size on its surface [21]. Subsequent work exploited the sub-wavelength size of photoconductive antennas to detect directly in the near-field of a collection aperture. These studies, being limited by the collection efficiency and frequency-dependent transmission of aperture probes, have led many to pursue apertureless (s-SNOM) near-field techniques [11].

Sub-micron resolution with THz-TDS was achieved for the first time in 2003 when a study using s-SNOM reported spatial resolution of 150nm at 2.0 THz [24]. This experiment was limited by a tip radius of 100nm, which is quite large by today's standards. Investigations into the frequency response of metal tips used in near-field THz-TDS revealed that tips reduce the bandwidth of near-field signal when compared to incident radiation bandwidth due to antenna effects [22]. Still, the technique continued to successfully resolve mesoscopic features. For example, one study mapped microdomains in vandium dioxide (VO_2) during its metal-insulator phase transition [23].

By 2008, resolution had improved to tens of nanometers. One publication at this time demonstrated an unprecedented 40nm resolution by mapping mobile carrier concentrations in semiconductor nanodevices. Using a 5mW THz beam incident on a tip with 30nm radius, this experiment distinguished the source, gate, and drain of a single Si transistor and enabled estimates of carrier concentrations in different regions based on measured THz plasmonic response [25]. Importantly, this experiment directly applied THz microscopy to characterize single nanodevices, which is a central goal for this technology. Subsequent experiments added temporal resolution to THz nano-microscopy using pump-probe techniques. A 2014 experiment used a 10fs pulse to excite electrons in an InAs nanowire, followed by THz radiation confined by s-SNOM, to trace the time-dependent dielectric function of the sample at different positions along the wire with 10nm resolution [26].

These foregoing studies applied near-field techniques to TDS studies, in which THz radiation is enhanced and confined by a tip over a sample, but generated elsewhere. We

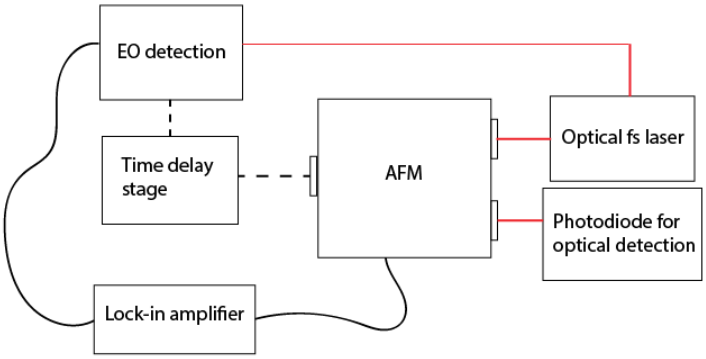

Figure 6: Schematic of nano-LTEM apparatus.

can think of these as "terahertz in, terahertz out" methods. Less work has been done to combine near-field optics with LTEM, though in 2014 one group did develop a near-field LTEM system using an aperture probe mounted on an AFM cantilever. That experiment, facing the limitations of aperture-based microscopy previously mentioned, yielded resolution of slightly less than 1 micron with the aid of solid immersion lenses [27]. No studies to date have combined s-SNOM with LTEM.

4 Methods and Materials

4.1 Nano-LTEM Experimental Design

This experiment represents the first realization of apertureless near-field LTEM, capable of mapping THz generation characteristics with nanoscale resolution. Major elements of the apparatus are depicted in Figure 6. At its heart is the AFM, which is enclosed in a casing with side ports for optical coupling and outgoing beam detection.

Through one port we pass in the optical femtosecond laser, which is mode-locked to a central wavelength of ≈820nm and full width at half maximum of ≈12nm. The repetition rate of this laser is 80MHz, and pulse widths are ≈100fs. A parabolic mirror mounted on an xyz-stage inside the AFM casing directs and focuses the optical laser to the tip. Tips used in this experiment are longer than conventional s-SNOM tips to provide clearance for longer wavelength THz radiation to propagate into the far field. These tips have 80μm shank

length, <20nm radius, and flexural resonances ≈20kHz. Tip oscillation and tip-sample separation are controlled by AFM software.

Another port provides access for optical detection. The ability to detect scattered 800nm light in real time is useful for coupling the femtosecond laser to the tip. Although optimizing optical near-field signal does not guarantee that LTEM signal will also be optimized, as tip-beam coupling differs for these signals, it is helpful to begin alignment here. Using an internal lock-in amplifier, the AFM software can display demodulated signal from the photodiodes or, alternatively, the THz detection system.

Outgoing THz radiation is detected through the third AFM port. To obtain a time trace of the emitted THz pulses, a retroreflector mounted on a translation stage serves as a time-delay system. Sweeping the position of the reflector, an external lock-in simultaneously records THz signal at the tip oscillation frequency, resulting in a near-field LTEM signal. The method used for actual THz pulse detection, electro-optic sampling, will be discussed in the next section.

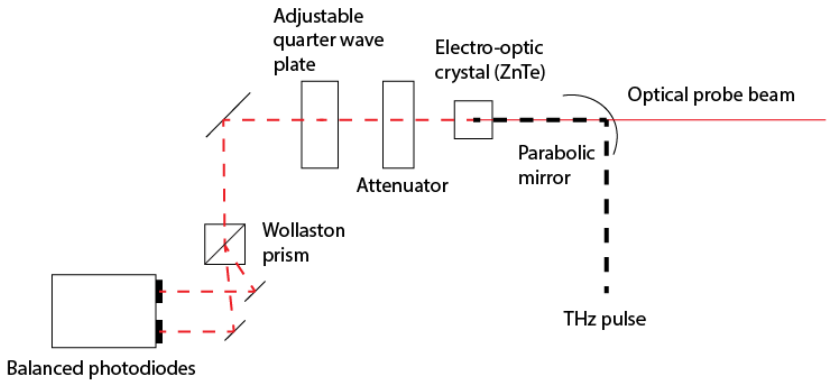

Figure 7: Schematic of electro-optic detection. Modulation of birefringence in 2mm ZnTe is used to measure THz pulse electric fields.

4.2 Electro-Optic Sampling

An alternative to detection via photoconductive antenna, eletro-optic (EO) sampling exploits the Pockels effect to visualize THz pulses. The refractive index of an EO crystal depends on polarization and propagation direction. Incident THz radiation instantaneously

modifies this birefringence, which is measured by observing the change in polarization state of an optical probe pulse. Essentially, we measure how THz radiation rotates the polarization of an optical beam in order to map the THz electric field.

Figure 7 shows a schematic of the optics used for EO sampling in this experiment. A parabolic mirror with a hole along its axis serves to combine THz emitted from the sample with a portion of the femtosecond optical beam used for LTEM, which then co-propagate through an EO crystal. After passing through an attenuator (to prevent detector saturation) and a quarter waveplate (which compensates for the equilibrium birefringence of the EO crystal), the modified optical beam encounters a Wollaston prism. This device separates light into two orthogonally polarized beams and directs them into two photodiodes.

The photodiodes are balanced by adjusting the quarter waveplate such that a zero voltage reading is produced in the absence of an incident THz field. Since these photodiodes operate at a rate of 125kHz, the pulsed 80MHz optical beam appears continuous. Difference in signal between the two detectors measures the degree of polarization rotation through the EO crystal, which is proportional to the THz electric field.

We use a 2mm thick ZnTe crystal as birefringent material in this experiment. Polarization of the incident THz and optical probe beams is oriented parallel to the [1, -1, 0] direction of the (110) ZnTe. The relatively large thickness of our crystal increases sensitivity by providing a greater interaction length, though it also creates a group-velocity mismatch which reduces the bandwidth of frequencies we can detect. In any near-field experiment, sensitivity is crucial, as measured signal levels are necessarily small, and so we deliberately trade some bandwidth for sensitivity.

4.3 Sample Characterization with TDS

Aiming to compare THz pulse emission from various semiconductor materials, we used TDS to characterize optical and electrical properties of our samples. The goal of these TDS measurements was to correlate spectroscopic responses of semiconductor wafers in the THz range with their THz emission properties. Unfortunately, as I describe below, this process proved to be more nuanced than originally anticipated.

We used a commercial TDS system (see Figure 3) with approximately 1.5THz bandwidth for these measurements. Initially, we pursued transmission mode TDS, in which obtaining a reference signal simply required removing the sample from the THz beam path. Figure 8

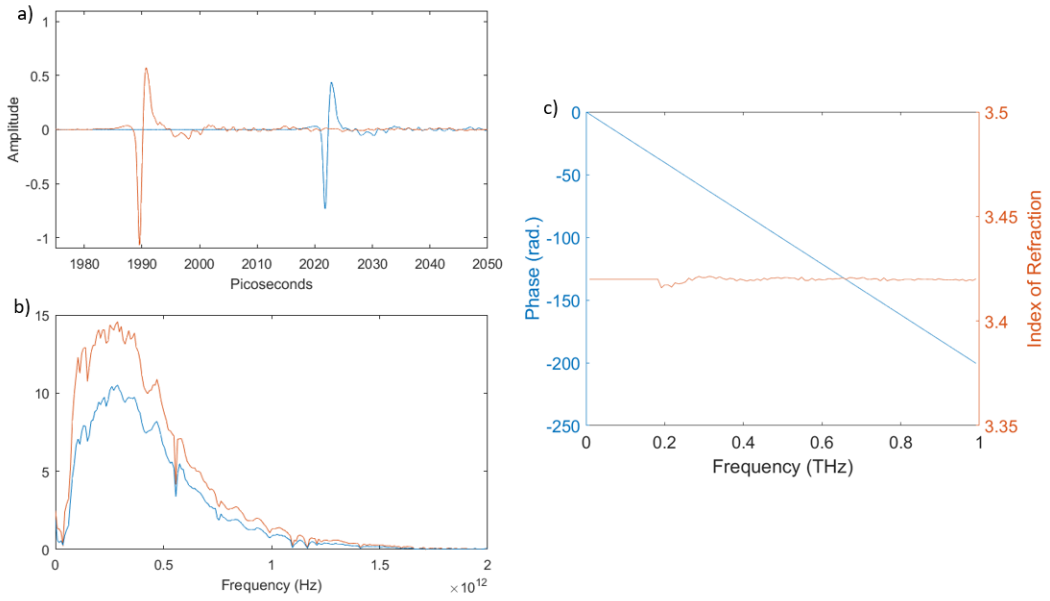

Figure 8: a) orange: reference signal, and blue: signal transmitted through semi-insulating silicon. b) spectra of signals in a). c) blue: unwrapped phase of reference-signal transfer function, and orange: calculated real part of index of refraction for semi-insulating silicon, 3.42.

shows an example of data collected on semi-insulating silicon, the index of refraction of which is well defined (real part, n = 3.42) in the THz regime. These results were obtained by first calculating the transfer function between sample and reference signals, then unwrapping the transfer function phase, and finally using Equations 3 and 4 to determine optical properties as functions of frequency.

Although this process yields correct results and could be used with other materials, we found that it was unable to extract optical information from the transmission TDS data we collected because our semiconductor materials were too optically thick. Highly doped semiconductors strongly absorb THz radiation, and thus transmitted THz signal recorded by the TDS system was too low to properly analyze.

Instead, we used reflection mode TDS, at $\theta_i = 45°$, to obtain a larger signal level. Reference signal was provided by a large mirror, which was then replaced by each semiconductor wafer in turn. To ensure that this placement was identical in angle and central position to

the placement of the reference mirror, two flat objects were used as a frame. By placing sample and mirror such that they were flush against this frame, we concluded that the placement was correct.

Close inspection of the measured THz pulse time traces, however, revealed that sample-reflected pulses arrived at the receiver more than half a picosecond before reference pulses. The obvious explanation for this phenomenon is that the frame-based positioning method failed in this case to ensure identical positioning of sample and mirror. According to [28], sample and reference mirror orientations should be the same to within mrads and surface positions the same within microns in order to ensure accuracy in analyzing relative phase shift of TDS data. Half a picosecond delay corresponds to 150 micron displacement. Although in [28] a correction for difference in pulse arrival time is used, this is a correction of less than 0.1 ps, which is significantly smaller than the discrepancy in this case.

Moreover, analysis of reflection TDS data that is not taken at normal incidence must consider THz pulse polarization, according to Equations 5 and 7. Since the transmitted THz beam in this case contained mixed polarizations (both s- and p-polarized light), it is difficult to draw any conclusions from the reflection TDS data.

These measurements ideally ought to be repeated with a more precise positioning methodology and with a polarizer in place to ensure that the Fresnel reflection coefficient can be accurately determined. Alternatively, normal incidence reflection could be used, with a beam splitter to direct back-reflected signal toward the THz receiver. In any case, the failure to appropriately characterize samples using TDS does not impact analysis of our nano-LTEM system, to which the following sections are dedicated.

5 Results and Discussion

5.1 Evidence of Near-field

By plotting higher harmonic signal as the oscillating AFM tip is retracted from a sample surface, we can check if the THz pulse we detect is actually near-field. To create this plot, we first find the position of the time-delay stage at which THz electric field is maximized and fix the stage here. Then, we gradually increase tip-sample separation. Since near-field signal exponentially decays away from the surface, we expect to see a drop in signal level in the first few tens of nanometers. As previously explained, higher harmonics of the

tapping frequency are better indicators of near-field than the first harmonic, which contains significant background signal. The approach curve shown in Figure 9 provides evidence that THz pulses measured while the AFM tip is in tapping contact are in fact near-field signals, as we measure a distinct cutoff at 37nm from the surface. This cutoff may be sharper than the exponentially decaying features seen in other s-SNOM approach curves because of strong plasmonic coupling of emitted THz radiation to the tip.

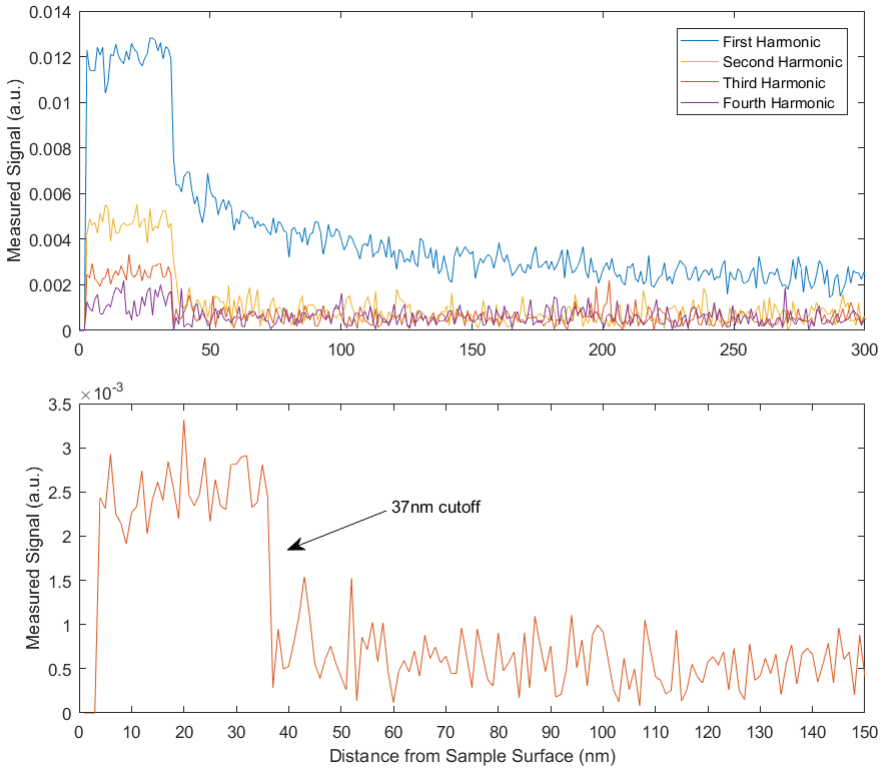

Figure 9: Approach curve taken over InAs ($N = 2 \times 10^{16}/\text{cm}^3$). Note that first harmonic signal includes a significant background level. Taking the third harmonic as a reliable near-field indicator, we find a $1/e$ cutoff at 37nm from the sample surface.

The tip-sample separation at which near-field signal decays should not be taken as a constant, as it is strongly dependent on tip sharpness. Sharper tips yield greater field enhancement and confinement, which leads to a stronger near-field signal and shorter decay length. Frustratingly, there is no way to measure tip sharpness during an experiment, and tips continuously degrade and are damaged during operation. Evidence that a tip

is damaged can sometimes be seen in 2D optical scans, where a blunt tip may introduce noticeable artifacts.

Approach curves such as Figure 9 are often used to estimate the spatial resolution of s-SNOM systems. Lateral resolution is commonly equated to the distance normal to the surface at which near-field signal levels drop by $1/e$. Using this definition and the approach curve in Figure 9, we might claim a spatial resolution of 37nm with the tip in the condition it was in while this approach curve was taken. In actuality, approach curves cannot be taken as indicators of lateral resolution in the case of LTEM because THz signal is generated from a nonlinear interaction with the sample rather than scattering.

In linear s-SNOM applications, incident radiation is simply scattered with amplitude determined by tip-sample coupling. LTEM, however, directly excites dipoles in the sample material to generate THz. This nonlinearity means that the apparent resolution in the direction normal to the sample surface may not reveal lateral resolution. To envision why, consider the mechanisms by which a tip may influence LTEM signal. In one case, an incident optical pulse impinges on the sample surface, photoexcites carriers, and the THz pulse emitted by these carriers scatters via near-field interaction into the far field by the tip. In another case, the optical pulse is enhanced and confined by the tip over a small region of the sample, photoexcites carriers, and then the carriers emit radiation into the far field. It remains an open question which of these processes is dominant in our experiment.

Another common way to determine spatial resolution is to scan the tip in a line across a sharp feature and measure the lateral distance over which signal drops. However, if this feature represents a sharp change in elevation as well as material, it may be difficult to interpret whether contrast is due to varying tip-sample distance or a difference in optical properties. For our experiment, an ideal test of resolution would be a line scan over a surface that is flat, with a sharp change in conductivity at a barrier. This scan could be followed by an approach curve with the same (sharp) tip to determine how the lateral and normal resolution of this instrument are related.

Even with lingering questions around defining spatial resolution, this nano-LTEM system has yielded THz emission images of gold nanoparticles on a GaAs substrate with resolution comparable to AFM topography (10-20nm). These results prove that this system is capable of achieving ultrahigh resolution for LTEM.

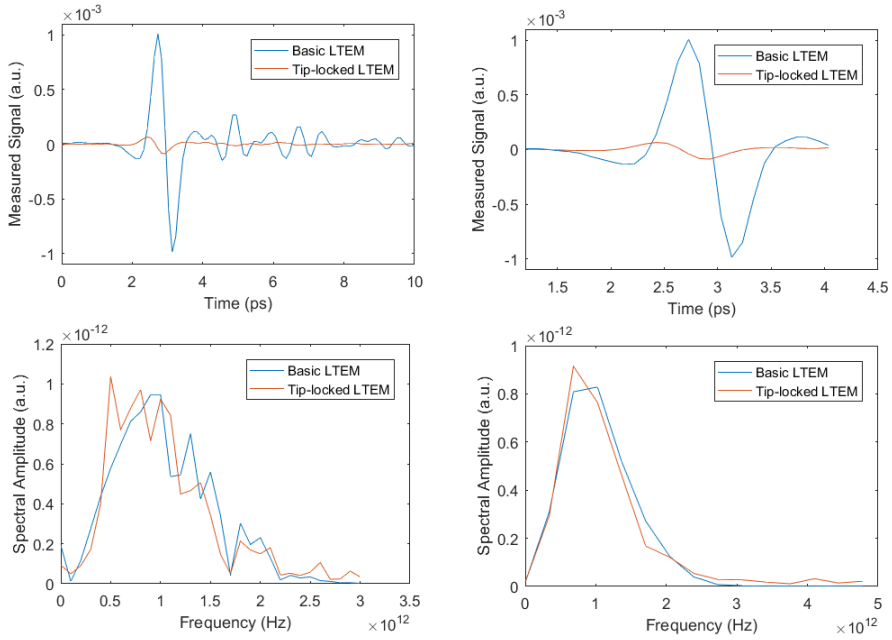

Figure 10: Left: Conventional and tip-locked LTEM signals from InAs ($N = 2 \times 10^{16}/cm^3$) in the time and frequency domains. Right: Windowing signals isolates the initial THz peaks, which yield very similar frequency spectra.

5.2 Conventional LTEM vs. Nano-LTEM

Comparing the results of this near-field LTEM system with conventional signals provides insight into what influence the presence of a tip has on THz pulse emission and detection. We expect a reduction in overall signal levels, as the volume of the sample being probed is significantly smaller, but there may also exist frequency-dependent differences in the amplitude and phase of detected pulses when a tip is present. As previously mentioned, the antenna response in an s-SNOM tip acts as a low-pass filter on detected near-field signal in the case of THz-TDS [22]. We would like to see if this type of antenna effect is also present in the case of near-field LTEM.

To acquire a conventional LTEM signal to compare with tip-locked signals, the sample stage is retracted from the tip, allowing the optical laser to simply impinge on its surface, and the rest of the experiment operates identically. Figure 10 displays THz pulses emitted

from an InAs wafer (N = $2.0\times10^{16}/\text{cm}^3$) in the conventional and tip-locked cases. As anticipated, the tip-locked signal amplitude is at least one order of magnitude smaller than the conventional LTEM signal. This discrepancy can also be explained by comparing power levels. The power delivered to the AFM tip cannot be so great as to damage the tip itself, while in the conventional LTEM case greater optical power may be used.

Importantly, frequency spectra for these two signals are very similar. The resemblance is particularly striking when comparing spectra for the initial THz pulse peaks only, as shown in Figure 10. Given these results, there does not appear to be a significant antenna effect when a tip is present, at least in the detected bandwidth. If there were, the transfer function formed by dividing these two normalized spectra would exhibit a $1/\omega$ dependence. Any enhanced out-coupling of radiation due to tip-sample interaction therefore occurs at the tip apex rather than along the shaft.

Material	Orientation	Thickness (μm)	Resistivity (Ω·cm)	Doping Concentration (cm^{-3})	Mobility ($cm^2/V\cdot s$)
n-InAs	[100]	350	0.01	2.0×10^{16}	>23,000
n-InAs	[100]	350	0.005	4.9×10^{16}	>21,000
n-GaAs	[111A]	400	0.0023	1.1×10^{18}	2500
p-GaAs	[100]	400	0.33	8.6×10^{16}	225
p-GaAs	[111B]	400	0.11	2.9×10^{17}	190-216
p-GaAs	[110]	500	0.2	1.27×10^{17}	245
n-Si	[100]	280	0.001-0.005	$\sim1\times10^{19}$	
p-Si	[100]	275	0.2-0.4	$\sim1\times10^{17}$	

Figure 11: Semiconductor materials investigated with nano-LTEM system.

5.3 Emission Differences by Material

Low-doped InAs exhibits strong THz pulse emission, which is why our foregoing discussion focused on this material. However, we also investigated other doped semiconductors materials to see which gave the best response in this system. Figure 11 summarizes the materials and their properties.

Carrying out both conventional and tip-locked LTEM measurements with the GaAs samples, we found that the conventional signal was already two orders of magnitude smaller than the signal from InAs pictured in Figure 10. No tip-locked signal could be isolated from background noise for these materials.

Surprisingly, the InAs ($N = 4.9\times10^{16}/cm^3$) sample did not emit THz pulses of amplitude anywhere near the less-doped InAs. Although we were able to isolate a tip-locked THz pulse from this sample, it was only after averaging five time traces together, each of which averaged every data point over nine seconds apiece. While it is true that larger carrier concentrations can lead to field screening which reduces emitted pulse amplitude [16], it is unusual that such a small difference in doping concentrations would lead to such a discrepancy in overall signal levels. We suspect that the doping concentrations listed by the wafer manufacturer may be inaccurate.

Silicon wafers were found to not emit THz pulses in either the conventional or tip-locked LTEM arrangements. This result is unsurprising, given the considerations discussed in section 2.2. Still, THz pulse emission may be possible with these samples if a voltage bias is applied between the tip and sample substrate. This voltage difference would supply an electric field that may accelerate enough photoexcited electrons to produce a THz pulse. InSb samples will also be tested in this system in the future.

As overall signal levels are dramatically reduced in nano-LTEM versus conventional LTEM, samples with quite high THz pulse emission are best candidates for future studies.

6 Conclusion

Our nano-LTEM system represents the first combination of apertureless near-field microscopy with terahertz emission microscopy. We found that the presence of a metal s-SNOM tip for LTEM studies does not exhibit an antenna effect that would reduce emission bandwidth, unlike in previous "THz in, THz out" studies. Analyses of tip-sample coupling can therefore treat the tip apex as a polarizable sphere and neglect the influence of the shaft. This methodology, common in other s-SNOM applications, simplifies interpretations of signal contrast during image acquisition. Successfully isolating near-field signal, we have achieved unprecedented (10-20nm) LTEM resolution. With this tool, we anticipate that terahertz emission across individual nanodevices can be probed and that ferroelectric domains, supercurrent distributions, and local electric fields can be mapped with nanoscale precision.

Acknowledgements

I would like to thank Professor Mittleman for advising me through this project, and all members of the terahertz group at Brown for their guidance and encouragement. Special thanks goes to Dr. Pernille Pedersen, who trained me on this experiment, and to my family for their unending support.

References

[1] L. Novotny and B. Hecht: Principles of Nano-Optics (Cambridge University Press, Cambridge, 2012).

[2] J.M. Atkin, S. Berweger, A.C. Jones, and M.B. Raschke: Nano-optical imaging and spectroscopy of order, phases, and domains in complex solids. Advances in Physics. **61** (6), 745-842 (2012)

[3] D.W. Pohl, W. Denk, and M. Lanz: Optical stethoscopy: Image recording with resolution $\lambda/20$. Appl. Phys. Lett. 44, 651-653 (1984)

[4] E.A. Muller, B. Pollard, and M.B. Raschke: Infrared chemical nano-imaging: Accessing structure, coupling, and dynamics on molecular length scales. J. Phys. Chem. Lett. **6**, 1275-1284 (2015)

[5] D.M. Mittleman: Frontiers in terahertz sources and plasmonics. Nat. Photonics **7**, 666–669 (2013)

[6] D.M. Mittleman (Ed.): Sensing with Terahertz Radiation (Springer, 2003)

[7] K. Sakai (Ed.): Terahertz Optoelectronics (Springer, 2005)

[8] T. Kampfrath, K. Tanaka, and K. Nelson: Resonant and nonresonant control over matter and light by intense terahertz transients. Nat. Photonics **7**, 680–690 (2013)

[9] J. Federici and L. Moeller: Review of terahertz and subterahertz wireless communications. J. Appl. Phys. **107**, 11 (2010)

[10] P.U. Jepsen, D.G. Cooke, and M. Koch: Terahertz spectroscopy and imaging - Modern techniques and applications. Laser Photonics Rev. **5**, 124–166 (2011)

[11] W.L. Chan, J. Deibel, and D.M. Mittleman: Imaging with terahertz radiation. Reports Prog. Phys. 70, 1325–1379 (2007)

[12] M. Tonouchi: Cutting-edge terahertz technology. Nat. Photonics **1**, 97–105 (2007).

[13] S. Nashima, O. Morikawa, K. Takata, and M. Hangyo: Measurement of optical properties of highly doped silicon by terahertz time domain reflection spectroscopy. Appl. Phys. Lett. **79**, 3923–3925 (2001)

[14] W. Withayachumnankul and M. Naftaly: Fundamentals of measurement in terahertz time-domain spectroscopy. J. Infrared, Millimeter, Terahertz Waves **35**, 610–637 (2014)

[15] P.G. Huggard, J.A. Cluff, G.P. Moore, C.J. Shaw, S.R. Andrews, S.R. Keiding, E.H. Linfield, and D.A. Ritchie: Drude conductivity of highly doped GaAs at terahertz frequencies. J. Appl. Phys. **87**, 2382 (2000)

[16] K. Liu, J. Xu, T. Yuan, and X.C. Zhang: Terahertz radiation from InAs induced by carrier diffusion and drift. Phys. Rev. B **73**, 1–6 (2006)

[17] P. Gu, M. Tani, S. Kono, K. Sakai and X.C. Zhang: Study of terahertz radiation from InAs and InSb. J. Appl. Phys. **91**, 5533–5537 (2002)

[18] J.N. Heyman, N. Coates, A. Reinhardt, and G. Strasser: Diffusion and drift in terahertz emission at GaAs surfaces. Appl. Phys. Lett. **83**, 5476–5478 (2003)

[19] H. Murakami and M. Tonouchi: Laser terahertz emission microscopy. Comptes Rendus Phys. **9**, 169–183 (2008)

[20] H. Murakami, U. Naotsugu, R. Inoue, S. Kim, T. Kiwa, and M. Tonouchi: Laser terahertz emission microscope. Proc. IEEE **95**, 1646–1657 (2007)

[21] S. Hunsche,M. Koch, I. Brener, and M. Nuss: THz near-field imaging. Opt. Commun. **150**, 22–26 (1998).

[22] K. Wang, D.M. Mittleman, N.C.J. Van Der Valk, and P.C.M. Planken: Antenna effects in terahertz apertureless near-field optical microscopy. Appl. Phys. Lett. **85**, 2715–2717 (2004)

[23] H. Zhan, V. Astley, M.l Hvasta, J.A. Deibel, Y.S. Lim, and D.M. Mittleman: The metal-insulator transition in VO2 studied using terahertz apertureless near-field microscopy. Appl. Phys. Lett. 91, 162110 (2007)

[24] H.T. Chen, R. Kersting, and G.C. Cho: Terahertz imaging with nanometer resolution. Appl. Phys. Lett. **83** (15), 3009-3011 (2003)

[25] A.J. Huber, F. Keilmann, J. Wittborn, J. Aizpurua, and R. Hillenbrand: Terahertz Near-Field Nanoscopy of Mobile Carriers in Single Semiconductor Nanodevices. Nano Letters. **8** (11), 3766-3770 (2008)

[26] M. Eisele, T.L. Cocker, M.A. Huber, M. Plankl, L. Viti, D. Ercolani, L. Sorba, M.S. Vitiello and R. Huber: Ultrafast multi-terahertz nano-spectroscopy with sub-cycle temporal resolution. Nature Photonics. **8** (11), 842-845 (2014)

[27] H. Murakami, K. Serita, Y. Maekawa, S. Fujiwara, E. Matsuda, S. Kim, I. Kawayama and M. Tonouchi: Scanning laser THz imaging system. J. of Phys. D: Appl. Phys. **47** (2014)

[28] T. Jeon and D. Grischkowsky: Characterization of optically dense, doped semiconductors by reflection THz time domain spectroscopy. Appl. Phys. Lett. **3032**, 5–8 (2009)